

# Coupled integrated photonic quantum memristors using a single photon source made of a colour center

Alessio Baldazzi<sup>1,\*</sup>, Roy Philip George Konnoth Ancel<sup>2,\*</sup>, Sebastiano Guaraldo<sup>1</sup>, Xuan Chen<sup>1</sup>, Ziad Abi Akar<sup>2</sup>, Regis Deturche<sup>2</sup>, Stefano Azzini<sup>1</sup>, Christophe Couteau<sup>2</sup>, and Lorenzo Pavesi<sup>1</sup>

<sup>1</sup>Department of Physics, University of Trento, Via Sommarive 14, Trento, 38123, Italy

<sup>2</sup>Laboratory Light, nanomaterials and nanotechnologies - L2n UMR 7076, University of Technology of Troyes-UTT and CNRS, 12 Rue Marie Curie, 10300 Troyes, France

\*These authors contributed equally to this work.

## Abstract

Photonic quantum memristors provide a measurement-induced route to nonlinear and history-dependent quantum dynamics. Experimental demonstrations have so far focused on isolated devices or simple cascaded devices configurations. Here, we experimentally realize and characterize a network of two coupled photonic quantum memristors with crossed feedback, implemented on a silicon nitride photonic integrated circuit and fed by a room-temperature single-photon source based on a silicon-vacancy color center  $\text{SiV}^-$  in a nanodiamond. Each memristor consists of an integrated Mach-Zehnder interferometer whose transfer function is adaptively updated by photon detection events on another memristor, thus generating novel non-Markovian input-output dynamics with an enhanced memristive behaviour compared to single devices. In particular, we report inter-memristor input-output hysteresis curves exhibiting larger form factors and displaying self-intersecting loops, respectively revealing marked bistability and topologically non-trivial memory dynamics. Furthermore, numerical simulations show how these features emerge from the interplay between memory depth and relative input phase, for both intra- and inter-memristor input-output relations. Our results establish coupled integrated photonic quantum memristors as scalable nonlinear building blocks and highlight their potential for implementing compact quantum neuromorphic and reservoir computing architectures.

## 1 Introduction

Machine learning has become one of the most powerful tools in industry, business, and daily life, enabling efficient data processing and decision-making [1, 2, 3]. Building on these successes, it is also increasingly adopted as an innovative tool in scientific research [4, 5, 6]. A key ingredient in machine learning is the presence of nonlinear transformations together with adaptive, state-dependent responses that provide memory, enabling learning and complex information processing. As efforts intensify to transfer these capabilities to the quantum domain, quantum machine learning has emerged as a promising direction with advantages for a broad class of problems, in particular for tasks that involve quantum data or quantum-generated correlations [7, 8, 9, 10, 11]. Yet, conventional quantum evolution is naturally unitary, and therefore inherently linear. As a result, realizing effective nonlinear dynamics typically relies on measurement-induced processes, open quantum systems, or feedback-based approaches [12, 13, 14]. Especially in quantum photonic systems, nonlinear interactions at the level of single photons are extremely challenging, as the requirements for their implementation are very demanding and still have to find a viable solution [15, 16, 17]. This motivates the search for alternative schemes that introduce nonlinearity in a more controllable and scalable manner.

In classical electronic hardware, nonlinearity and memory features are naturally combined within a single element, the memristor, a resistor whose resistance depends on the history of the applied current, thus incorporating memory of past inputs [18, 19]. Memristors provide an efficient physical implementation of synaptic functionality and have become key components in the search and development of new neuromorphic computing architectures [20, 21]. Inspired by these developments, quantum memristors have been introduced as an architectural solution for neuromorphic quantum computation, providing a controlled way to realize effective nonlinearity [22]. The nonlinearity is introduced by correlating the evolution with its past measurement outcomes. At the same time, the dependence of its response on previous measurement outcomes gives rise to memory effects, thus enabling history-dependent input-output relations.

Quantum memristors have been investigated theoretically across multiple physical platforms, including superconducting circuits [23], trapped ions [24] and quantum dots [25], where they have also been experimentally explored. In parallel to these developments, photonic platforms have attracted growing interest due to their intrinsic advantages, such as low decoherence, room-temperature operation, and ultrahigh bandwidth, together with their natural compatibility with large-scale integrated photonic architectures [26, 27, 28, 29]. These characteristics make photonics particularly well suited for implementing measurement-based adaptive dynamics and memory-dependent quantum processes [30, 31]. Early photonic quantum memristors (PQMs) were based on a tunable beam splitter, whose reflectivity is adaptively updated according to measurement outcomes [32]. This scheme established the fundamental operating principle of PQMs and has recently been extended to more complex architectures, such as cascaded PQMs [33]. Building upon this foundational concept, subsequent work introduced a dual-rail encoding approach [34], which permits the implementation of a photonic quantum memristive behavior using Mach-Zehnder interferometers (MZIs), a standard building block of photonic integrated circuits (PICs), thereby facilitating the extension of PQMs toward larger-scale implementations. Crucially, this particular implementation expands the prospects of investigating novel PQMs configurations and PICs based on them. Indeed, on the one hand, improvements in PICs, such as low-loss waveguides with ultrahigh bandwidth, offer the opportunity to build large-scale and high-efficiency information processing units [35, 36, 37], while on the other hand, high-performance single photon sources exist, such as diamond color centers, that can offer near deterministic single photon emission at room temperature, alleviating experimental demands and enabling potential on-chip integration [38, 39, 40].

In this work, we report on the experimental investigation of two coupled PQMs with crossed feedback implemented on a silicon nitride PIC and fed by a single-photon source based on a  $\text{SiV}^-$  color center in nanodiamonds operating at room-temperature. Silicon vacancy  $\text{SiV}^-$  color centers feature a narrow emission peak (in contrast to nitrogen-vacancy centers  $\text{NV}^-$ ) thanks to which they have already demonstrated their versatility across several quantum technologies, including solid-state quantum memories [41, 42, 43] and elementary quantum networks [44], where single photons emitted by  $\text{SiV}^-$  centers act as flying qubits interfacing distant spin-based nodes. Beyond networking, the availability of stable and spectrally narrow single-photon emission makes  $\text{SiV}$ -based sources potentially well-suited for linear optical quantum computing architectures, where indistinguishable photons are a fundamental resource for multi-photon interference. Using single photons from our nanodiamond-based single  $\text{SiV}^-$  color center, we characterize both inter- and intra-memristor input-output relations, observing enhanced memory effects and more complicated effective nonlinear responses. Our results considerably extend the relevance of PQMs beyond isolated devices, enabling their exploration in networked architectures with complex connectivity and memory-induced entanglement dynamics [45, 46, 47]. In this context, suitably interconnected quantum memristors enabled by integrated photonics offer a physically grounded and scalable route toward quantum neural networks and photonic quantum simulators [48, 49, 50]. This work constitutes the first implementation of PQMs combining memristive devices and a quantum light source both characterized by a high level of

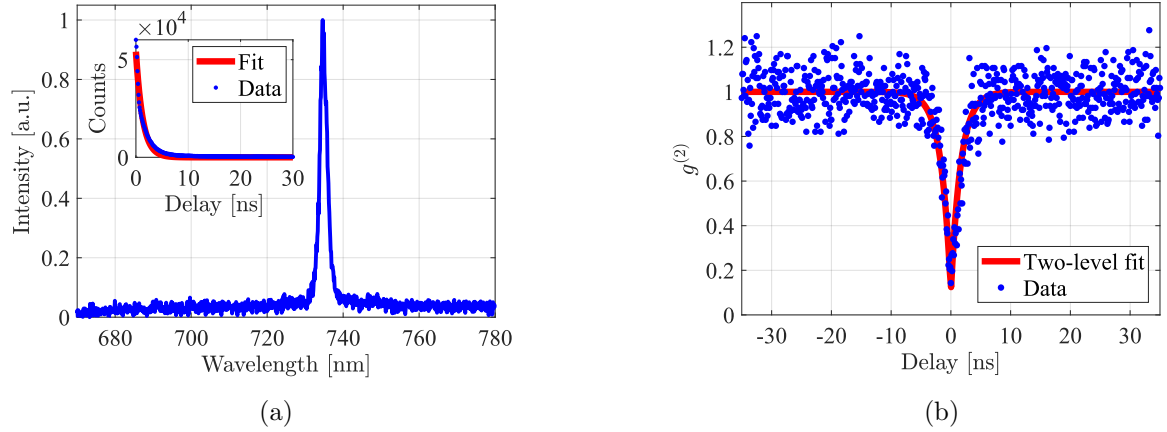


Figure 1: (a) The photoluminescence spectrum of the  $\text{SiV}^-$  showing a sharp ZPL peak at 734 nm. In the inset, the time decay of the photoluminescence (points) and its single exponential fit (line). The fit yields a lifetime of the  $\text{SiV}$  of 1.89 ns. (b) Second order correlation data (points) of the emitted photons as a function of the time delay between the two arms of the HBT interferometer. Data are fitted by a two levels model (line) which evidences a clear photon antibunching behaviour.

integrability, thus paving the way towards large-scale PQMs architectures.

The paper is structured as follows. Section 2 introduces the single photons source. Section 3 describes the photonic implementation of a single PQM and two coupled PQMs. In Section 4, we present and discuss the experimental results. Finally, Section 5 draws the conclusions and reports a comparison with the other implementations of photonic quantum memristors reported so far.

## 2 Single photons source

To study the behaviour of coupled photonic quantum meristors, single photons from a negatively charged silicon vacancy  $\text{SiV}^-$  color center were coupled to the input of the integrated circuit. Color centers are defects created or naturally present in the all-carbon lattice of diamond when adjacent carbon atoms are replaced by a vacancy-impurity atom combination that exhibits an atom-like electronic structure [51, 52]; in the case of  $\text{SiV}^-$ , this impurity is a Silicon atom. The so-called group-IV color centers, such as the  $\text{SiV}^-$ , exhibit bright, narrow-band, highly polarized and photostable single photon emission with short lifetimes [53, 54]. In the  $\text{SiV}^-$  color center, a silicon atom occupies an interstitial split-vacancy position between two adjacent empty lattice sites, giving the  $\text{SiV}^-$  color center an inversion symmetry arising from the lack of a permanent electric dipole, which also shields the  $\text{SiV}^-$  from electrical noise in its vicinity. The  $\text{SiV}^-$  is a spin half system with ground and excited state levels that have partially lifted degeneracies due to spin-orbit coupling. The ground state sub-levels are separated by a splitting of 50 GHz while the excited state splitting is around 260 GHz. The zero phonon line (ZPL), which corresponds to the electronic transition between the excited and ground state, has a narrow peak at 737 nm in contrast to the better known nitrogen-vacancy center  $\text{NV}^-$ , which is characterized by a broad emission due to a strong phonon coupling [52].

The  $\text{SiV}^-$  used in this work is hosted in a nanodiamond grown using a high pressure and high temperature (HPHT) process [55]. This specific nanodiamond was selected from among those deposited on a silicon substrate via spin coating. The selection process was conducted using a homemade room temperature micro-photoluminescence ( $\mu$ -PL) setup by means of confocal intensity scans followed by photoluminescence measurements. For this specific  $\text{SiV}^-$ , we

obtained a spectrum showing the ZPL to be at 734 nm as shown in Fig. 1(a). We attribute the deviation from the standard  $\text{SiV}^-$  ZPL at 737 nm to the strain experienced by the color center within the nanodiamond, what we observed in other nanodiamonds [56]. The  $\mu$ -PL setup used to characterize the color center is described in more detail in Appendix A. The inset of Fig. 1(a) presents the time decay of the photoluminescence from which we estimated a lifetime of  $1.89 \pm 0.02$  ns. The single photon emission was confirmed using a Hanbury Brown and Twiss interferometer with the measurement of the photon autocorrelation function  $g^{(2)}(0)$  showing an antibunching dip of  $0.098 \pm 0.032$  and a FWHM (full width at half maximum) of  $2.25 \pm 0.11$  ns. These data were obtained by a fit of the experimental points with a 2-level emitter model (red curve in Fig. 1(b)). The FWHM value is consistent with the measured lifetime. The  $g^{(2)}(0)$  value is limited by the background light coming from the untreated surface of the nanodiamond. The  $\mu$ -PL optical setup was coupled to a single mode fiber yielding a briigtness at the fiber output of 170 kcps. All measurements were initially performed at the University of Technology of Troyes (UTT), where the emitter position was recorded relative to the silicon substrate corners using a homemade triangulation protocol (see Appendix B for more details). This enabled the  $\mu$ -PL setup to be disassembled, transported to the University of Trento, and rapidly reassembled while reliably relocating the same emitter (see Appendix A). As a result, the triangulation protocol effectively enabled the portability of the single-photon source.

### 3 Integrated photonic quantum memristors

The memristor concept was first proposed by Chua in the 1970s [18, 57] as a fundamental circuit element that relates magnetic flux and electric charge, as predicted by symmetry considerations in nonlinear electrical circuits. A memristor was demonstrated for the first time in 2008 with a nanoscale electronic circuit by Strukov et al. [58]. The notion of memristive systems was soon extended to capacitive and inductive elements [59]. Nowadays, it has been made clear that memelements are physical devices that satisfy specific physical properties [19]. In a general form, the memristive behavior can be described by

$$y = f(s, x, t)x, \quad \dot{s} = g(s, x, t), \quad (1)$$

where  $x$  and  $y$  denote the input and output variables, respectively,  $s$  represents the internal state of the memristor, and  $f$  and  $g$  are functions that depend on the input, time, and the system's previous states. This formulation explicitly captures both the nonlinear response and the memory effect of the device: the output  $y$  depends on the input  $x$  through a state-dependent function  $f(s, x, t)$ , while the evolution of the internal state  $s$  is driven by the past and present values of the input, giving rise to history-dependent dynamics and hysteresis effects. With the aim of extending the concept of a classical memristor to the quantum regime, the most direct approach is to promote classical variables to quantum observables, while ensuring that the evolution remains coherent to preserve genuinely quantum features. However, the defining characteristics of a memristor—nonlinearity and memory effects—necessarily require non-Markovian dynamics, which cannot arise from closed, unitary evolution alone. This naturally calls for a description in terms of open quantum systems, where controlled measurement processes or environment-induced back-action provide a physically consistent mechanism to generate history-dependent and nonlinear responses. While this framework captures the essential requirements for a quantum memristor, realizing it in practice remains a significant experimental challenge.

In photonic platforms, a PQM, can be implemented using a beam splitter [32] or an MZI [34], which are denoted as single- and dual-rail devices, respectively. In the latter scheme, as shown in Fig. 2(a), a photonic qubit is encoded in the path degree of freedom of the two upper modes A and B. The input state is in superposition:

$$|\psi_{\text{in}}(t)\rangle \equiv \alpha(t)|1_A, 0_B\rangle + \beta(t)|0_A, 1_B\rangle, \quad (2)$$

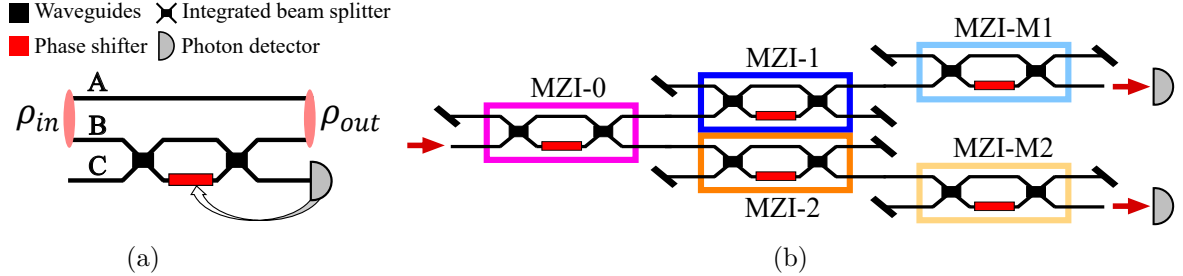


Figure 2: (a) Dual-rail scheme of the photonic quantum memristor, where the input state  $\rho_{in}$  is encoded as a single photon in a superposition of the upper path modes A-B. The component in mode B is transformed by the Mach-Zehnder interferometer, implementing the photonic quantum memristor, while the component in mode A propagates freely to the output state  $\rho_{out}$ . The Mach-Zehnder interferometer is composed of two beam splitters (black rectangles), and a phase shifter (red rectangle). The output on mode C is used as a feedback for the phase setting of the memristor. (b) Schematic layout of the circuit implementing a single (MZI-M1) and two coupled integrated photonic quantum memristors (MZI-M1 and MZI-M2)). The red arrow on the left indicates the input waveguide, while the arrows on the right are placed to highlight the output waveguides, fiber-coupled to single-photon SPAD detectors. MZI-0, MZI-1, MZI-2 are used to prepare the suitable input state for the PQM. The input and output waveguides that are not used in the experiments are pointed out by a black oblique line.

and the input density matrix is  $\rho_{in}(t) \equiv |\psi_{in}(t)\rangle\langle\psi_{in}(t)|$ , where the qubit state  $|0_{A/B}\rangle$  corresponds to zero photons in mode A/B and  $|1_{A/B}\rangle$  corresponds to a photon in mode A/B. Then, an auxiliary mode C without photons is added to the input state, giving the total state  $|\psi_{in}(t)\rangle\otimes|0_C\rangle$ , and the transformation  $U(t)$  associated to the MZI acting on modes B and C is applied, i.e.  $U(t)\rho_{in}(t)\otimes|0_C\rangle\langle 0_C|U(t)^\dagger$ . Given the input state and denoting the reflectance of the MZI as  $R(t)$ , the MZI map reads:

$$U(t) = \mathbf{1}_A \otimes \left[ |0_B, 0_C\rangle\langle 0_B, 0_C| + \sqrt{1 - R(t)} |1_B, 0_C\rangle\langle 1_B, 0_C| + \sqrt{R(t)} |0_B, 1_C\rangle\langle 1_B, 0_C| + \sqrt{1 - R(t)} |0_B, 1_C\rangle\langle 0_B, 1_C| - \sqrt{R(t)} |1_B, 0_C\rangle\langle 0_B, 1_C| \right], \quad (3)$$

where  $\mathbf{1}_A$  is the identity map over the mode A. Note that our convention implies that a 'transmitted photon' is a photon entering in mode B/C and remaining in mode B/C after the MZI with probability  $1 - R(t)$ , while a 'reflected photon' is a photon entering in mode B/C and exiting in mode C/B with probability  $R(t)$ . The output density matrix  $\rho_{out}(t)$  is defined as the partial trace over the mode C of the density matrix  $U(t)\rho_{in}(t)\otimes|0_C\rangle\langle 0_C|U(t)^\dagger$ . This means that

$$\begin{aligned} \rho_{out}(t) &\equiv \langle 0_C | U(t) \rho_{in}(t) \otimes |0_C\rangle\langle 0_C| U(t)^\dagger |0_C\rangle + \langle 1_C | U(t) \rho_{in}(t) \otimes |0_C\rangle\langle 0_C| U(t)^\dagger |1_C\rangle \\ &= \left( \alpha(t) |1_A 0_B\rangle + \beta(t) \sqrt{1 - R(t)} |0_A 1_B\rangle \right) \left( \bar{\alpha}(t) \langle 1_A 0_B| + \bar{\beta}(t) \sqrt{1 - R(t)} \langle 0_A 1_B| \right) \\ &\quad + |\beta(t)|^2 R(t) |0_A 0_B\rangle\langle 0_A 0_B|. \end{aligned} \quad (4)$$

The average input photon number in mode B is  $\langle N_{in}(t) \rangle \equiv \text{Tr} [\rho_{in} \mathbf{1}_A \otimes |1\rangle_B\langle 1|_B] = |\beta(t)|^2$  and the corresponding output average photon number  $\langle N_{out}(t) \rangle \equiv \text{Tr} [\rho_{out} \mathbf{1}_A \otimes |1\rangle_B\langle 1|_B] = [1 - R(t)]\langle N_{in}(t) \rangle$ . Finally, the quantum memristor is implemented by an MZI acting on mode B and an auxiliary mode C through the tunable beam-splitting reflectance  $R(t)$  of the MZI, which is related to the phase setting of the MZI. Thus, looking at Eq. (1),  $(\langle N_{in} \rangle, \langle N_{out} \rangle)$  correspond to  $(x, y)$ , and  $R$  plays the role of the internal memristive state  $s$ , which is controlled by previous measurement outcomes. This measurement process effectively couples the device to an environment and renders the dynamics non-unitary. In fact, the measurement outcomes

are used to update the internal state variable  $R(t)$ , such that its evolution depends on the past output of the system. As a consequence, the current input–output relation is conditioned on the system’s history, realizing a genuinely non-Markovian dynamics. Since the component in mode A propagates freely to the output state  $\rho_{out}$  and only the component in mode B participates in the memristive feedback dynamics, the evolution of the quantum memristor can be fully characterized by the dynamics of the measurable input and output average photon numbers,  $\langle N_{in}(t) \rangle$  and  $\langle N_{out}(t) \rangle$ . These observables can be evaluated from the photon flows on output spatial modes A, B and C. In particular,  $\langle N_{in}(t) \rangle$  can be found from the average photon flow on output mode C divided by  $R(t)$ .

To illustrate the basic operating principle, the nonlinearity and memory effects of the memristor can be probed by observing the emergence of a hysteresis loop [32]. This requires a cyclic driving protocol in which the input variable is swept from small to large values and back again, such that the output depends not only on the instantaneous input but also on its history. For this reason, the input photon number  $\langle N_{in}(t) \rangle$  is chosen to vary sinusoidally between zero and a maximum value  $\langle N_{max} \rangle$  according to  $\langle N_{in}(t) \rangle = \sin^2(\pi t/T_{osc})$ , where  $T_{osc}$  is the oscillation period and all photon numbers are normalized by the maximum value  $\langle N_{max} \rangle$ . The reflectance  $R(t)$  is updated by the following relation:  $\dot{R}(t) = \langle N_{in}(t) \rangle - 0.5$ , similarly to Eq. (1). The resulting dynamics of  $R(t)$  can then be written as [34]:

$$R(t) = \frac{1}{2} + \frac{1}{T} \int_{t-T}^t \left( \langle N_{in}(t') \rangle - \frac{1}{2} \right) dt' \quad (5)$$

Here, the integration window  $T$  defines the memory depth of the quantum memristor, characterizing how many past input states contribute to the current internal state. Our experiments with the single memristor and the coupled memristors are performed in  $N$  time bins of temporal duration  $\tau$ . Starting from the time bin duration, the characteristic times are  $T_{osc} = M_{osc}\tau$  and  $T = M\tau$ , with  $(M_{osc}, M)$  being integers. The first one is related to the period of the sinusoidal oscillation of the input photon flux, while the second one is related to the buffer length of the memristor. Each time bin  $t_k$  is associated to an input  $\langle N_{in}(t_k) \rangle$  evaluated from the number of detected photons on output modes B and C divided by the total number of detected photons on all the output modes. Analogously, the output  $\langle N_{out}(t_k) \rangle$  is found from the number of detected photons on output modes B divided by the total number of detected photons on all the output modes. The feedback law in Eq. (5) becomes

$$R(t_k) = \frac{1}{2} + \frac{1}{M} \sum_{j=k-M+1}^k \left( \langle N_{in}(t_j) \rangle - \frac{1}{2} \right). \quad (6)$$

$R(t_k)$  is then translated in a specific phase setting of the MZI implementing the PQM during the time bin  $t_k$ . In our experiments, we chose  $\tau = 20$  s plus the dead times due to electrical communications and phase settings of the MZIs. This time allows to collect enough detector’s counts in order to estimate the observables  $\langle N_{in}(t_k) \rangle$  and  $\langle N_{out}(t_k) \rangle$ .

Importantly, the integrated photonics paradigm makes this approach particularly appealing: MZIs constitute a standard and highly controllable building block in photonic integrated circuits (PICs), allowing compact, stable, and reproducible implementations. As a result, this architecture naturally supports scalability, enabling the extension from single memristive elements to large networks of coupled quantum memristors. The PIC used for this work is contained in a silicon nitride chip, and the waveguides are designed to be single-mode (cross-section 550 x 150 nm<sup>2</sup>). Multimode-interference-based integrated beam splitters (MMIs) [60] are optimized to work with the fundamental transverse electric field (TE<sub>0</sub>). The integrated MZIs are made of two MMIs and a pair of phase shifters, one above each waveguide of the MZI’s arms [61]. Fig. 2(b) shows the schematic PIC layout. The circuit is composed of two sections: a triangular scheme of three MZIs, denoted as MZI-0, MZI-1 and MZI-2, and two parallel MZIs denoted

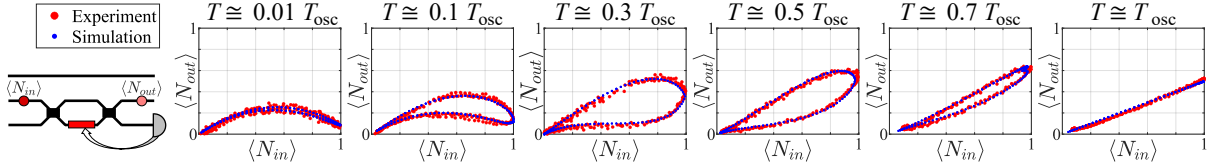


Figure 3: Experimental and simulation results of a single photonic quantum memristor with different ratios between the two time scales: oscillation period of the modulated input flux,  $T_{\text{osc}}$ , and time length of the memristor’s buffer,  $T$ . On the left, a schematic diagram of the device is shown.

as MZI-M1 and MZI-M2. We inject the single photons into the second input waveguide of MZI-0 (counting from the top, see red arrow). Then, only the second outputs of MZI-M1 and MZI-M2 (counting from the top, see red arrows) are connected to fiber-coupled single-photon silicon avalanche diode (SPAD) detectors. The choice of the output channels is related to the properties of the MZIs: the transmission on the two outputs of MZIs is related by a  $\pi/2$  phase shift, thus we can effectively sample both outputs by collecting photons at the same output channel with two different phase settings and two runs. This implies the doubling of the time of the experiments, but it allows the use of fewer detectors and outputs, which are generally characterized by different coupling losses.

In the case of the single-memristor experiments, MZI-0 is used to modulate the photon flux to the upper output with a sinusoidal shape in time, while MZI-1 and MZI-2 are set to transmit all the light to the upper and lower outputs, respectively. MZI-M1 is the integrated memristor, while MZI-M2 is used in a fixed setting to transmit all the photons on its lower output to compute the average photon numbers. In the coupled-memristor experiments, MZI-M1 and MZI-M2 serve as the integrated memristors working in parallel with independent input modulations. MZI-0 evenly splits the input flow between its upper and lower outputs, while MZI-1 and MZI-2 modulate the photon flux entering the two memristors with a sinusoidal time dependence. We choose the buffer length of both memristors to be equal to  $M$ , and we introduce a relative phase shift  $\Phi$  between the time modulation of MZI-1 and MZI-2. Only two detectors are used in this case as well, by exploiting the  $\pi/2$  phase shift between the outputs of each MZI (see Appendix C for details). The feedback laws for MZI-M1 and MZI-M2 are given by:

$$R^{(1)}(t_k) = \frac{1}{2} + \frac{1}{M} \sum_{j=k-M+1}^k \left( \langle N_{in}^{(2)}(t_j) \rangle - \frac{1}{2} \right), \quad R^{(2)}(t_k) = \frac{1}{2} + \frac{1}{M} \sum_{j=k-M+1}^k \left( \langle N_{in}^{(1)}(t_j) \rangle - \frac{1}{2} \right), \quad (7)$$

where the superscript refers to the first or second memristor. Thus, the setting of one memristor depends on the history of the other, and vice versa.

## 4 Results and discussions

Using the single-photon source described in Section 2 and the PIC presented in Section 3 [62], the experiments with a single PQM and two parallel PQMs with crossed feedback laws are executed for different configurations. In particular, for both cases the ratio between  $T_{\text{osc}}$  and  $T$  is varied, while in the second case also the phase shift between the input single photon fluxes is changed. Before every measurement, we run a calibration routine of all the used integrated devices, namely the MZIs highlighted in Fig. 2(b). The calibration gives not only the relation between the phase and the electrical power of each thermal phase shifter, but also the interference visibilities of the associated MZI. Due to the insertion losses of the PIC (20dB) and the single-photon rate of the source (170 kcps), in-fiber polarization control of the input signal is not feasible. In addition,

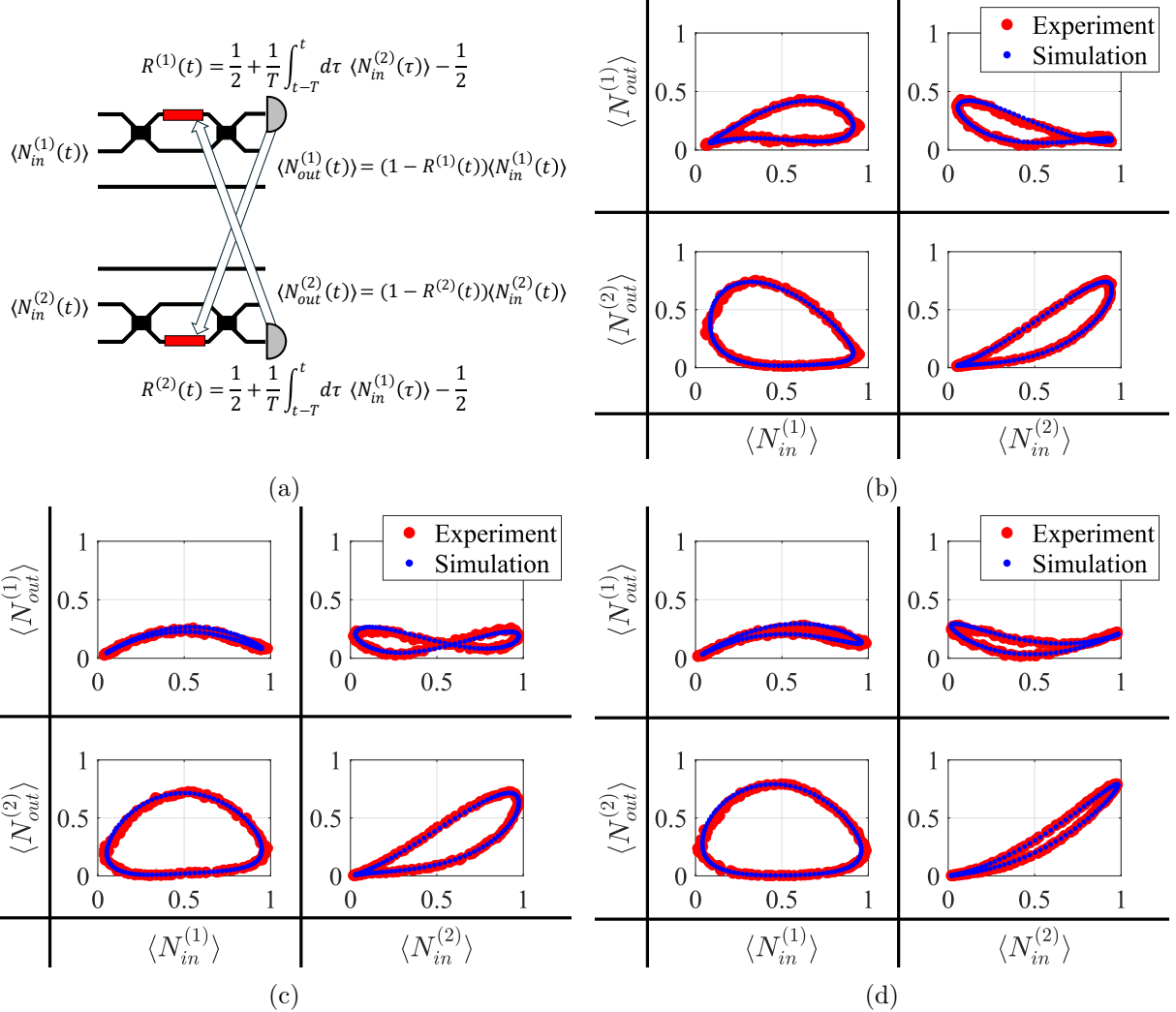


Figure 4: (a) Schematic representation of the coupled photonic memristors with crossed feedbacks whose relations are described in integral form. Eq. (7) shows the corresponding discrete version. (b-d) Experimental and simulation results of coupled photonic quantum memristors for different ratios  $T/T_{osc}$  and input phase difference  $\Phi$ . Both single photonic quantum memristors receive a sinusoidal input with the same period  $T_{osc}$  and they have the same buffer length  $T$ . In particular, (b)  $T = 0.2 T_{osc}$  and  $\Phi = 0.7\text{rad}$ . (c)  $T = 0.3 T_{osc}$  and  $\Phi = 0.5\text{rad}$ . (d)  $T = 0.4 T_{osc}$  and  $\Phi = 0.7\text{rad}$ . The four panels refer to the intra (diagonal cells) and inter (off-diagonal cells) memristor relations.

alignment of the single-photon source is performed by adjusting a non-polarization-maintaining output fiber and directly coupling it to the SPAD detectors. As a result, the polarization state of the injected photons can change after each realignment, requiring recalibration of the MZIs, which are polarization-sensitive. Indeed, as they are designed to operate in the  $\text{TE}_0$  mode, any  $\text{TM}_0$  component in the guided light reduces the visibility of the interference they produce.

Fig. 3 presents the results for a single PQM. We set  $T_{osc} = 100\tau$ . Depending on the ratio between the two characteristic times,  $T_{osc}$  and  $T$ , different input-output curves arise. When  $T = 0.01 T_{osc} = \tau$ , the average input flux  $\langle N_{in} \rangle$  at previous times does not enter in the feedback law, and the input-output relation is almost a parabola, first curve in Fig. 3. For  $\tau < T < T_{osc}$  (second to fifth curves in Fig. 3), the input-output curve is characterized by a hysteresis figure pinched at the origin<sup>1</sup>, while remaining nonlinear. Finally, for  $T = T_{osc}$  the input-output

<sup>1</sup>A hysteresis figure is pinched at a point when its ascending and descending branches are tangent to each

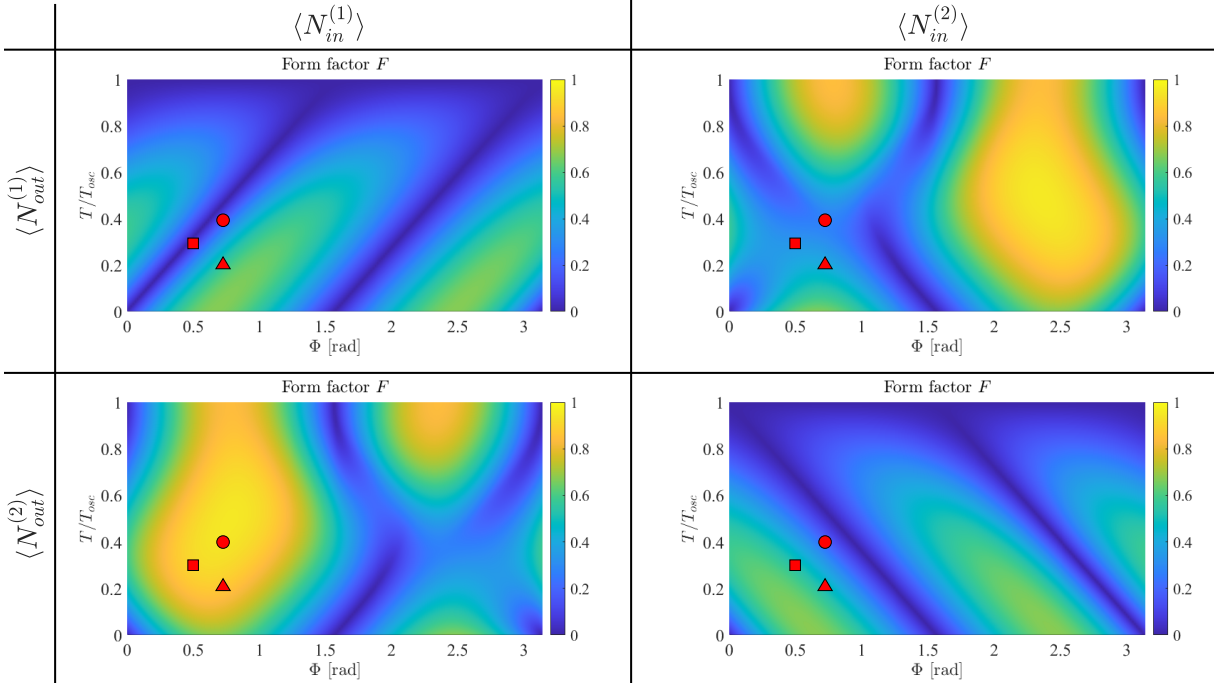


Figure 5: Simulations of the form factor  $F$  of the intra- and inter-memristor hysteresis curves of two coupled photonic quantum memristors with crossed feedbacks as a function of the relative phase  $\Phi$  between their inputs and the ratio  $T/T_{\text{osc}}$  between the buffer length of the memristors,  $T$ , and the period of the sinusoidal input modulation,  $T_{\text{osc}}$ . The form factor  $F$  is  $4\pi$  times the ratio between the area and the squared perimeter of the hysteresis curve. The intra-relations,  $(\langle N_{\text{in}}^{(1)} \rangle, \langle N_{\text{out}}^{(1)} \rangle)$  and  $(\langle N_{\text{in}}^{(2)} \rangle, \langle N_{\text{out}}^{(2)} \rangle)$ , are on the diagonal of the table, and the inter-relations,  $(\langle N_{\text{in}}^{(2)} \rangle, \langle N_{\text{out}}^{(1)} \rangle)$  and  $(\langle N_{\text{in}}^{(1)} \rangle, \langle N_{\text{out}}^{(2)} \rangle)$ , are on the off-diagonal. The red symbols in the surface plots indicate the choice of parameters used in the experiments of the two coupled memristors with crossed feedback reported in Fig. 4: in particular, the triangle-square-circle represents the choice associated with the hysteresis curves in Fig. 4(b-c-d), respectively.

relation becomes temporally punctual (memory effect is lost) and linear, last curve in Fig. 3. These behaviours are analogous to the electric case [18, 58], since the feedback law considers the average of the input flux over a full period. Together with the experimental data, numerical simulation results are also reported (the blue curves). In the simulations results reported in Fig. 3 (see Appendix D for details), the non-unitary visibilities extracted from the calibration routine are included for all the MZIs used in the experiments.

In the case of the coupled PQMs, we choose the times  $(T_{\text{osc}}, T)$  of both devices to be equal, and we set  $T_{\text{osc}} = 100\tau$ , as in the single-memristor case. Within this configuration, we studied the dependence of the input-output relations with respect to the ratio  $T/T_{\text{osc}}$  and to the relative phase  $\Phi$  between the sinusoidal inputs. The outcome is simply the one of two independent PQMs for zero phase difference, while non-trivial intra- and inter-memristor relations between the input-output fluxes arise for a non-zero phase difference. Here and in the following, we refer to  $(\langle N_{\text{in}}^{(i)} \rangle, \langle N_{\text{out}}^{(i)} \rangle)$  as intra-relations, with  $i = \{1, 2\}$ , and to  $(\langle N_{\text{in}}^{(i)} \rangle, \langle N_{\text{out}}^{(j)} \rangle)$  as inter-relations, with  $i, j = \{1, 2\}$  and  $i \neq j$ . Fig. 4 shows the experimental results, together with simulations with the real visibilities, for different configurations of inputs' phase difference  $\Phi$  and ratio  $T/T_{\text{osc}}$ . Appendix D contains the parameters of the simulations. We observe that peculiar hysteresis figures can be obtained for inter-relations, sharing the common feature of not being pinched at the origin. In particular, Figs. 4(b-c-d) show 'large area' curves for  $(\langle N_{\text{in}}^{(1)} \rangle, \langle N_{\text{out}}^{(2)} \rangle)$

other in this point [19].

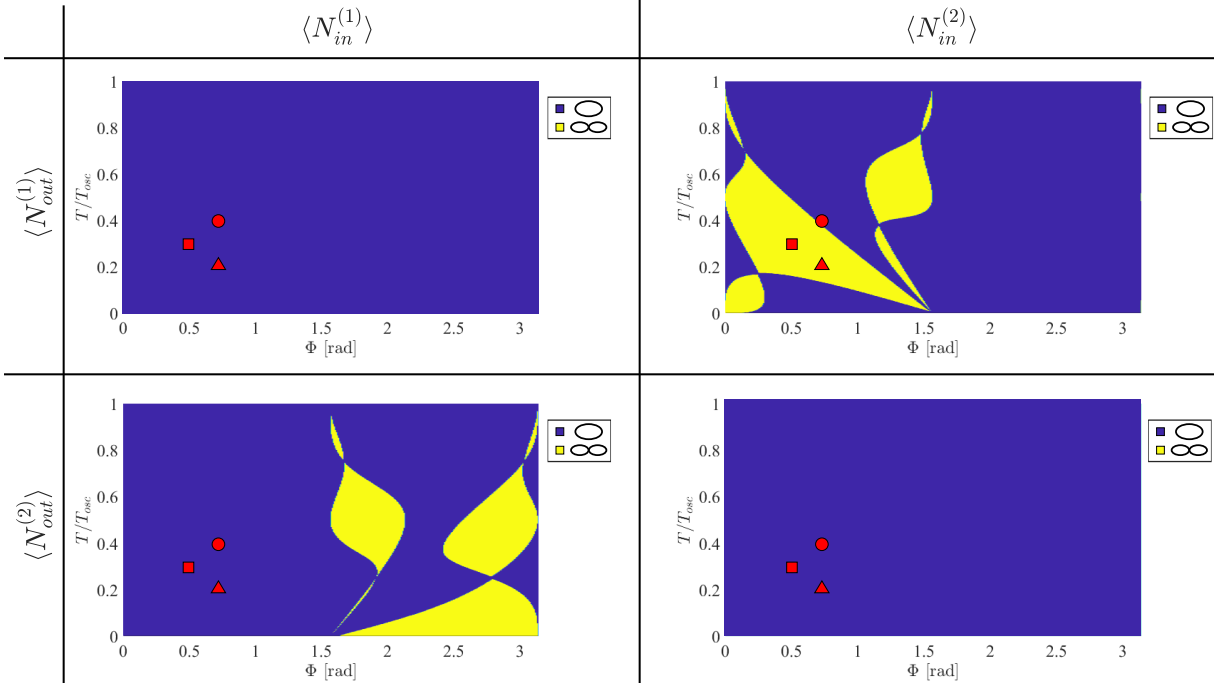


Figure 6: Simulations results revealing the presence (yellow regions) of a self-intersecting hysteresis loop in two coupled PQMs with crossed feedback as a function of the relative phase  $\Phi$  between the inputs and the ratio  $T/T_{osc}$  between the buffer length of the memristors,  $T$ , and the period of the sinusoidal input modulation,  $T_{osc}$ . The infinity symbols and the yellow stands for self-intersecting curves, while the ellipse and the blue for not-self-intersecting curves. The red symbols in the surface plots indicate the choice of parameters used in the experiments of the two coupled memristors with crossed feedback reported in Fig. 4: in particular, the triangle-square-circle represents the choice associated with the hysteresis curves in Fig. 4(b-c-d), respectively.

and 'infinity loop'-like self-intersecting curve for  $(\langle N_{in}^{(2)} \rangle, \langle N_{out}^{(1)} \rangle)$ . The former type of hysteresis curve is interestingly characterized by the fact of featuring a marked bistable behaviour. While the second aspect, to the best of our knowledge, has not been reported for electrical memelements yet: a self-intersection point implies that the derivative of the curve is not unique and the curve is topologically non-trivial. These features agree with former observations reporting that non-pinched hysteresis loop under periodic drive can be found e.g. in several electrical devices with memory [19].

Relevant features of the hysteresis curves of coupled PQMs are their overall size and the presence of a point of self-intersection. The first aspect is quantified by the form factor  $F$ , which is equal to  $4\pi A/P^2$ , where  $A$  and  $P$  are the area and the perimeter of the hysteresis curve, respectively. We investigated both features in numerical simulations by varying the relative phase  $\Phi$  between the input fluxes and the ratio  $T/T_{osc}$  between the buffer length of the memristors and the period of the sinusoidal modulation of the inputs. Fig. 5 shows the form factor for the four hysteresis curves  $(\langle N_{in}^{(1/2)} \rangle, \langle N_{out}^{(1/2)} \rangle)$  with different choices of  $\Phi$  and  $T/T_{osc}$ . For the intra-relations, there are constant-level lines of the form factor. The points indicated with the red square and circle/triangle in Fig. 5 share the same value of form factor: this is manifest by looking at the corresponding intra-relations in Fig. 4(c) and Fig. 4(d)/(b), respectively. Very interestingly, the maxima of the form factor of the hysteresis curves of intra-relations, namely  $(\langle N_{in}^{(1)} \rangle, \langle N_{out}^{(1)} \rangle)$  and  $(\langle N_{in}^{(2)} \rangle, \langle N_{out}^{(2)} \rangle)$ , have value  $\approx 0.67$  for  $T/T_{osc} \ll 1$  and relative phases equal to  $\Phi \approx (0.65, 2.47)$  rad. So, even if the single memristors have a buffer with only one element, the largest form factor arises from the correlations due to the crossed feedback, Eq. (7), and specific values of phase shift  $\Phi$  between the input single photon fluxes.

The form factors of the inter-relations,  $(\langle N_{in}^{(2)} \rangle, \langle N_{out}^{(1)} \rangle)$  and  $(\langle N_{in}^{(1)} \rangle, \langle N_{out}^{(2)} \rangle)$ , have maximum of  $\approx 0.95$  for  $T/T_{osc} \approx 0.5$  and relative phases  $\Phi \approx 2.35$  rad and  $\Phi \approx 0.77$  rad, respectively. Moreover, the form factor of the inter-relations has a maximum higher than the form factor obtained with a single memristor, i.e.  $F \approx 0.58$  for  $T/T_{osc} \approx 0.35$ , which is a clear indication of enhanced bistable behaviour. Fig. 6 reports the map of the regions where a self intersection point can be observed in the hysteresis curves as a function of  $\Phi$  and  $T/T_{osc}$ . Note that there are no self-intersecting curves for the intra-relations, while several choices of  $\Phi$  and  $T/T_{osc}$  produce a self-intersecting point for only one inter-relation curve. Indeed, a self-intersection point for one inter-relation curve excludes a self-intersection point for the other inter-relation curve.

## 5 Conclusions

We have successfully implemented one and two coupled photonic quantum memristors on a compact and small-scale silicon nitride photonic chip, by using an off-chip silicon vacancy color center as a source of single photons, and external SPAD detectors. All components operate at room temperature and ambient pressure. Table 1 summarizes a comparison with other implementations of one or two photonic quantum memristors reported in the literature, showing that our work is the only one using a deterministic source and memristive elements both working at room temperature. Despite our nanodiamond-based source of single photons is off-chip, the deterministic coupling of  $\text{SiV}^-$  color centers [40, 39], as well as their direct integration [63, 64] in silicon nitride photonic circuits has been already reported, thus providing to our demonstration a perspective of full integration and scalability. Nevertheless, a still open challenge remains in the integration of multiphoton sources to increase the system's dimensionality. While large scale PICs are already a reality, indistinguishable and pure single-photon sources based on colour centers are still under development and require low temperature [65].

	[34, 48]	[33]	This work
number of memristors	1	1 and 2 (cascaded)	1 and 2 (in parallel)
photon source	collinear Type II SPDC (heralding)	quantum dot [66]	$\text{SiV}^-$ color center
memristor implementation	FLW-waveguides in silicate glass [67]	bulk optical setup	Silicon nitride PIC
working temperature	$\sim 300$ K	$\sim 4$ K (the source)	$\sim 300$ K

Table 1: Comparison of photonic quantum memristor experiments in terms of the number of devices, the type of source, the photonic platform used for the implementation, and working temperature. FLW stands for femtosecond-laser written, and SPDC for spontaneous parametric down conversion.

Our single PQM measurement results reproduce very closely those reported in [34], where a bulk crystal was instead employed to generate single photons via spontaneous parametric downconversion followed by heralding. Moreover, we present experiments of two coupled PQMs featuring a cross-feedback law. The results show different hysteresis curves, depending on the fact that intra- or inter-memristor relations are considered, characterized by novel features, among them: non-pinched behaviour, enhanced form factor and non-trivial topology (self-intersection). Our experiments clearly highlight an interesting response of these devices as building blocks for quantum neural networks. Indeed, the correlations introduced in the crossed feedback laws, Eq. (7), can enhance the non-linearity and the history-dependent response of the overall structure. The presented simulations make manifest the richness of the new dynamics, arising from the classical correlations between the memristors and their inputs.

These results mark a step forward towards integrated photonic quantum neuromorphic computing built by means of universal MZI schemes [68, 69] and photonic quantum memristors [34]. Indeed, the synaptic weights of the network can be introduced through the linear manipulation of MZI networks, while the non-linearity and memory effects through the action of different photonic quantum memristors. In particular, having shown that crossed feedback laws of two memristors modify the input-output intra- and inter-memristor relations, paves the way to the creation of more complex networks with fewer resources. Two independent memristors working in parallel with different buffer lengths cannot reproduce the same relations due to the lack of correlations between their internal states. Instead, crossed feedback laws give rise to non-trivial features even for memristors working in parallel. Thus, by using dependent and independent memristors, higher non-linearity and enhanced memory-dynamics can be achieved in e.g. recently proposed reservoir computing schemes [49] by following the approach first suggested by [34], whose capabilities rely on the richness of the network.

## Method

The  $\text{SiV}^-$  emitter used in this work is hosted in an HPHT-grown nanodiamond [55] spin-coated onto a silicon substrate. A suitable single emitter was selected with a home-made room-temperature  $\mu$ -PL confocal setup by performing intensity scans followed by spectral and photon-correlation measurements. The spectrum shows a ZPL at 734 nm (Fig. 1(a)), and single-photon emission was confirmed with a Hanbury Brown and Twiss interferometer, yielding  $g^{(2)}(0) = 0.098 \pm 0.032$  after a two-level fit (Fig. 1(b)). The  $\mu$ -PL output was coupled to a single-mode fiber, providing a count rate of  $\sim 170$  kcps. To ensure reproducible relocation after transport, the emitter position was recorded relative to substrate reference corners and recovered using our home-made triangulation protocol (Appendix A) after reassembling the portable  $\mu$ -PL setup. This enabled a relocatable, fiber-coupled single-photon source for coupling into the photonic circuit containing the memristors.

The photonic circuit was made via a photolithographic process through a commercial service provided by Ligentec SA. The waveguides are made of a silicon nitride core, 150 nm thick and 550 nm wide, embedded in a silica cladding. This cross-section ensures single-mode propagation at wavelengths around 750 nm. In our setup using a standard fiber array at the output, the total insertion loss of the photonic circuit is around 20 dB. An electrical power supply (Qontrol systems - BP8 device model) is used to provide the currents for the phase shifters of the PIC. The input photons are injected into the photonic circuit using a tapered lensed fiber. Two silicon-based single-photon avalanche diodes (SPADs, Excelitas), with equal detection efficiencies and dark counts, are used together with time-tagging electronics (Swabian Instruments), which are interfaced with a PC for detection events acquisition. The total input photon flux is around  $10^2$  kHz, while the output flux is around 1 kHz. We chose a time bin of 2 s and 20 s, denoted as  $\tau$ , during the calibration routine and the memristor experiments, respectively.

The experimental setup is described in more detail in the Appendix A.

## Acknowledgements

We are grateful for financial supports from Horizon Widera 2023 (101160101) through ToEQPL project. R.P.G.K.A. and C.C. are grateful for financial supports from the EUR NANO-PHOT (ANR 18-EURE-0013) as well as the Region Grand Est and the OQuLus PEPR project (ANR 22-PETQ-0013).

## Author contributions

A.B. and R.P.G.K.A. contributed equally to this work. R.P.G.K.A., and R.D. performed the optical characterization of the single photon source at UTT using a  $\mu$ -PL setup. R.P.G.K.A. and Z.A.A. assembled a similar more portable  $\mu$ -PL setup at University of Trento and used the home-made triangulation protocol to find the same Single photon emitter. A.B., R.P.G.K.A., S.G., X.C., Z.A.A. carried out the memristors' experiments. A.B. and S.G. analysed the results of the memristors' experiments and performed the simulations. S.A., C.C. and L.P. provided critical feedback and helped shape the research, analysis and manuscript.

## Competing interests

The authors declare no competing financial interests.

## Appendix

### A Setup

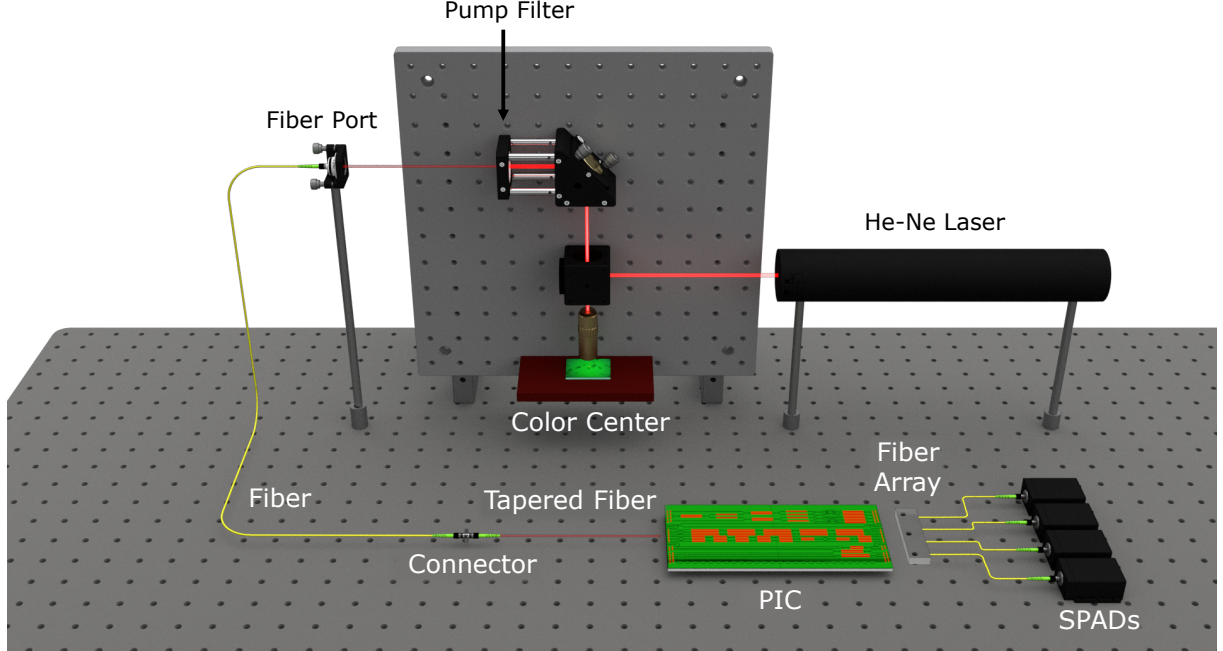


Figure 7: A simplified image of the setup.

The PL and correlation measurements were made at UTT using a 633 nm Helium Neon laser to excite the  $\text{SiV}^-$  through a 100X air objective with numerical aperture of 0.95 for optimal collection of the emitted photons. The laser is first directed to a pellicle beam splitter with a reflection/transmission ratio of 8:92. Part of the laser is reflected to the objective, as shown in Fig. 7. The focused laser beam excites the  $\text{SiV}^-$  and the fluorescence is collected by the same objective and sent to the collection path via a flipping mirror that allowed to choose between a spectrometer or a HBT setup. A laser cleanup filter (Semrock LL01-633-25) was placed along the illumination path to the sample while a long-pass filter at 647 nm (Semrock LP02-647RU-25) was used along the collection path to reject the laser. An additional narrowband filter at 740 nm (Semrock FF01-740/13-25) was also used for the HBT experiments. The setup assembled at the University of Trento for the experiments reported in this work (see Fig. 7) follows a similar design, with the only change being the laser source, which was a 640 nm diode laser. A clean-up filter (Semrock VersaChrome 704/13 tunable bandpass filter) was used immediately after the laser and the same filter combination as on the collection path of the setup at the UTT was used at the end of the collection arm to reject the laser. A fiber port was used to couple the collected emission to a single mode fiber that fed the PIC. Optical coupling at the chip's input is performed through a tapered lensed fiber, while output coupling is realized using a standard fiber array. An electrical power supply (Qontrol systems - BP8 device model) provides the currents for all the phase shifters (PSs) of the PIC. Single photons are detected by silicon SPADs (Excelitas), all featuring the same efficiencies and dark counts. Finally, the output counts are managed by a fast time-tagging electronics (Swabian Instruments) connected to a PC.

## B Triangulation

This a technique we developed to reliably locate previously identified single photon emitters on the substrates. It is based on an inspection camera and on nano-positioner stages. Our protocol consists of two main parts: acquiring the reference frame information and then imposing a transformation on it. In the initial frame of reference, the  $(x, y)$  coordinate readout from the nanopositioner stages are recorded for at least 3 reference points  $(x_1, y_1)$ ,  $(x_2, y_2)$  and  $(x_3, y_3)$ , which are usually chosen to be any clear and sharp feature near the corners of the substrate, and for the point of interest  $(x_p, y_p)$ .

A linear transformation corresponds to the relocation of the sample with the emitter in a new setup. First, we make sure that the same reference points can be retrieved after the linear transformation by recording images of each reference corner with the exact sharp feature made to coincide with the center of the camera crosshair overlay. Then, we readout the new set of coordinates  $(x'_1, y'_1)$ ,  $(x'_2, y'_2)$  and  $(x'_3, y'_3)$  for each of the reference points. These are used to get the coordinates of the point of interest in the new transformed reference frame.

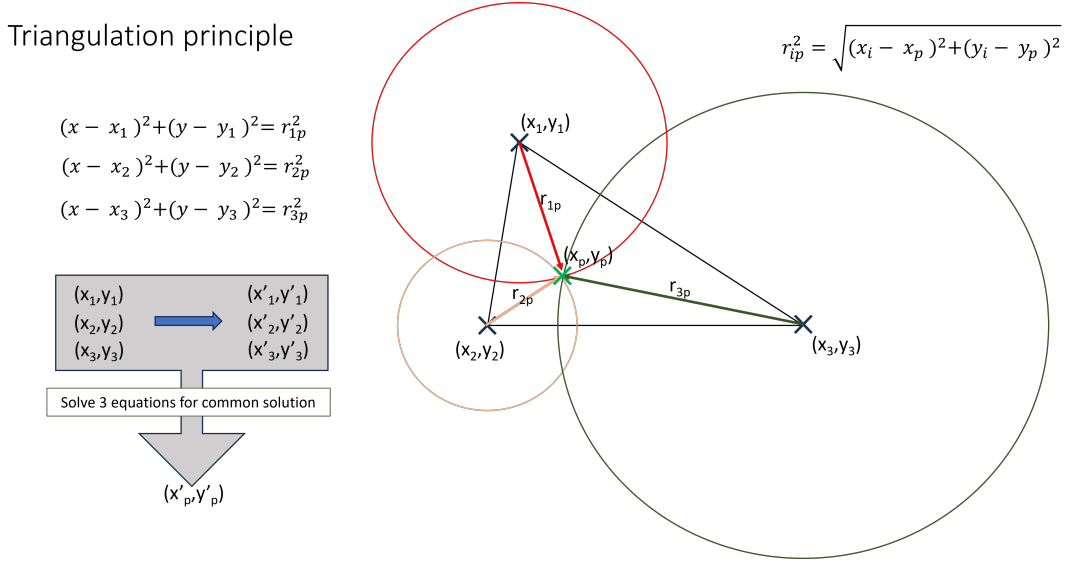


Figure 8: The basic principle behind triangulation.

The reference points in the old frame can be thought of as the centers of three circles whose radii equal their respective distances from the point of interest  $(x_p, y_p)$ . The Euclidean distance can easily be calculated for each of the three distances  $r_{1p}$ ,  $r_{2p}$  and  $r_{3p}$ , as shown in Fig. 8. With these radii, the equations of the three circles can be defined, as shown in Fig. 8. The relation between these four points remains the same even after the linear transformation, which means that we now have the same set of three circles in the new frame, with different centers but the same radii. Solving these three equations for a common solution gives the coordinates for the point of interest  $(x'_p, y'_p)$  in the new frame of reference, since three non-concentric circles can intersect at only one point. Finally, the nano-positioner stages move to this point and the emitter should be within the field of view of the inspection camera.

There are limitations to this technique, particularly when it comes to emitters with dimensions smaller than the diffraction limit. While the reference coordinates corresponding to the corners can still easily be acquired, it is difficult to zero in on the nano-emitter which cannot be resolved on the inspection camera. Another problem is the accuracy, repeatability and positional instability or drift of the nanopositioner stages. A quick work around for these problems is to use triangulation to arrive in the neighborhood of the emitter and then proceed with a confocal scan to find it.

## C Procedures for memristors experiments

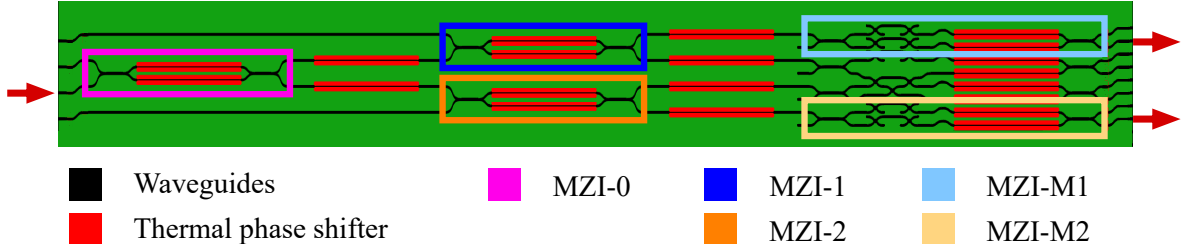


Figure 9: The layout of the circuit implementing single memristor and two coupled memristors. Only the highlighted Mach Zehnder interferometers (MZIs) are utilized. The arrow on the left indicates the input waveguide (third one from the top), while the arrows on the right are placed to highlight the output waveguides (the second and eighth ones from the top), fiber-coupled to single-photon avalanche diodes.

Fig. 9 shows the schematic layout of the used PIC, which features four input and eight output waveguides. The circuit is composed of two sections: a triangular scheme of three MZIs, denoted as MZI-0, MZI-1 and MZI-2, and a network composed of MMIs, crossing waveguides and phase shifters, containing MZIs denoted as MZI-M1 and MZI-M2. This circuit was originally designed to implement a swap test on a generic state of two qubits based on single-photon path encoding [62]. In Appendix E of [62], the characterization curves of MMIs are reported.

We utilize only the MZIs highlighted in Fig. 9. We choose to inject the single photons into the third input waveguide (counting from the top of the layout), and collect them with a fiber array. Only the second and eighth output waveguides (counting from the top) are connected to fiber-coupled single-photon silicon avalanche diode (SPAD) detectors.

In the single-memristor experiments, the following steps are performed within each time bin  $t_k = k\tau$  with  $k \in [0, N - 1]$  (refer to Fig. 9):

1. Set the MZI-0 to modulate the input flux with transmission equal to  $\sin^2(\pi t_k/T_{\text{osc}})$ , and set MZI-1 and MZI-2 to transmit all the photons to the upper and lower output, respectively.
2. Set the MZI-M1 implementing the memristor with phase  $\theta_k$ , which corresponds to transmission to its lower output waveguide equal to  $R(t_k)$ , and set MZI-M2 to transmit all the photons to the eighth output waveguide.
3. Collect single-photon detection events at the detectors fiber-coupled to the two output waveguides for  $\tau_{\text{meas}} < \tau$ .
4. Set the MZI-M1 implementing the memristor with phase  $\theta_k + \pi/2$ , corresponding to transmission to the lower output waveguide equal to  $1 - R(t_k)$ .
5. Collect single-photon detection events at the detectors fiber-coupled to the two output waveguides for  $\tau_{\text{meas}} < \tau$ .
6. Evaluate  $\langle N_{\text{in}}(t_k) \rangle$ ,  $\langle N_{\text{out}}(t_k) \rangle$ , and update the phase setting of the memristor MZI-M1 according to the chosen feedback law.
7. Return to step 1.

In the first time bin, the parameter  $R$  of the memristor is set to zero, and the memristor buffer is composed of a null vector of dimension  $M$ . After  $M$  time bins, the buffer is completely filled, and new entries are saved by keeping the last  $M$  entries (LIFO). After the buffer is full, the memristor starts to show hysteresis. This procedure could be implemented with just one

detector by exploiting the  $\pi/2$ -relation of the MZI modulating the input. However, in order to reduce the duration of the measurement, for the single-memristor case two output waveguides are measured. Instead, for the coupled memristors case, only one output channel per memristor is used. The input and output averaged photon fluxes are

$$\langle N_{in}(t_k) \rangle = \frac{N_2(\theta_k) + N_2(\theta_k + \pi/2)}{N_{tot}(t_k)} , \quad \langle N_{out}(t_k) \rangle = \frac{N_2(\theta_k + \pi/2)}{N_{tot}(t_k)} , \quad (8)$$

where  $N_{tot}(t_k) = N_2(\theta_k) + N_2(\theta_k + \pi/2) + N_8(t_k)$ ,

where  $N_2(\theta_k)$  and  $N_2(\theta_k + \pi/2)$  are the number of detector's clicks at the second output during the step 3 and 5 of the  $k$ -th time bin, respectively, while  $N_8(t_k)$  the number of detector's clicks at the eighth output during step 3. The feedback law for MZI-M1 is

$$R(t_k) = \frac{1}{2} + \frac{1}{M} \sum_{j=k-M+1}^k \left( \langle N_{in}(t_j) \rangle - \frac{1}{2} \right) , \quad (9)$$

which is the same used in the first implementation of a photonic quantum memristor [34].

In the coupled-memristor experiments, the following steps are performed within each time bin  $t_k = k\tau$  with  $k \in [0, N - 1]$  (refer always to Fig. 9):

1. Set MZI-0 to equally split the input flow to its two outputs, and set MZI-1 and MZI-2 to modulate the input fluxes with transmission equal to  $\sin^2(\pi t_k/T_{osc})$  and  $\sin^2(\pi t_k/T_{osc} + \Phi)$ , respectively, where  $\Phi$  is a phase difference between the two inputs.
2. Set MZI-M1 and MZI-M2 with phases  $\theta_k^{(1)}$  and  $\theta_k^{(2)}$ , which correspond to transmission to their lower output waveguides equal to  $R^{(1)}(t_k)$  and  $R^{(2)}(t_k)$ , respectively.
3. Collect single-photon detection events for  $\tau_{meas} < \tau$  from the two output waveguides.
4. Set MZI-M1 and MZI-M2 with phases  $\theta_k^{(1)} + \pi/2$  and  $\theta_k^{(2)} + \pi/2$ , which correspond to transmission to their lower output waveguides equal to  $1 - R^{(1)}(t_k)$  and  $1 - R^{(2)}(t_k)$ , respectively.
5. Collect single-photon detection events for  $\tau_{meas} < \tau$  from the two output waveguides.
6. Set MZI-1 and MZI-2 with transmission equal to  $\cos^2(\pi t_k/T_{osc})$  and  $\cos^2(\pi t_k/T_{osc} + \Phi)$  respectively (both have  $\pi/2$ -shift with respect to step 1), and set MZI-M1 and MZI-M2 to transmit all the photons to the lower output waveguides, outputs two and eight respectively.
7. Collect single-photon detection events for  $\tau_{meas} < \tau$  from the two output waveguides.
8. Evaluate  $\langle N_{in}^{(1)}(t_k) \rangle$ ,  $\langle N_{out}^{(1)}(t_k) \rangle$ ,  $\langle N_{in}^{(2)}(t_k) \rangle$ ,  $\langle N_{out}^{(2)}(t_k) \rangle$  and update the settings of the memristors according to the chosen feedback law.
9. Return to step 1.

The described procedure uses the minimum number of detectors, one per memristor. Also in this case, the parameter  $R$  of the memristor is initially set to zero, the memristors buffer is made of a null vector of dimension  $M$ , and new entries in the buffers are saved by keeping the last  $M$

entries (LIFO). The input and output averaged photon fluxes are

$$\begin{aligned}\langle N_{in}^{(1)}(t_k) \rangle &= \frac{N_2(\theta_k^{(1)}) + N_2(\theta_k^{(1)} + \pi/2)}{N_{tot}^{(1)}(t_k)} , \quad \langle N_{out}^{(1)}(t_k) \rangle = \frac{N_2(\theta_k^{(1)} + \pi/2)}{N_{tot}^{(1)}(t_k)} , \\ \langle N_{in}^{(2)}(t_k) \rangle &= \frac{N_8(\theta_k^{(2)}) + N_8(\theta_k^{(2)} + \pi/2)}{N_{tot}^{(2)}(t_k)} , \quad \langle N_{out}^{(2)}(t_k) \rangle = \frac{N_8(\theta_k^{(2)} + \pi/2)}{N_{tot}^{(2)}(t_k)} ,\end{aligned}\quad (10)$$

where  $N_{tot}^{(1)}(t_k) = N_2(\theta_k^{(1)}) + N_2(\theta_k^{(1)} + \pi/2) + \bar{N}_2(t_k)$ ,  
and  $N_{tot}^{(2)}(t_k) = N_8(\theta_k^{(2)}) + N_8(\theta_k^{(2)} + \pi/2) + \bar{N}_8(t_k)$ ,

where  $N_{2/8}(\theta_k^{(1/2)})$  and  $N_{2/8}(\theta_k^{(1/2)} + \pi/2)$  are the number of detector's clicks at the second/eighth output during the step 3 and 5 of the  $k$ -th time bin, respectively, while  $\bar{N}_{2/8}(t_k)$  the number of detector's clicks at the second/eighth output during step 7.

## D Simulations of the experiments

The memristor consists of a MZI. Its reflectivity ideally should follow the law [34]:

$$R_{mem}(t_k) = \frac{1}{2} + \frac{1}{M} \sum_{j=k-M+1}^k \left( \langle N_{in}(t_j) \rangle - \frac{1}{2} \right) . \quad (11)$$

Practically,  $R$  is set by imposing a relative phase  $\phi$  between the two arms of the MZI:

$$R = \sin^2 \left( \frac{\phi}{2} \right) . \quad (12)$$

The ideal average values  $\langle N_{in} \rangle$  and  $\langle N_{out} \rangle$  read as follows

$$\begin{aligned}\langle N_{in}(t_k) \rangle &= \sin^2 \left( \frac{\phi^{in}(t_k)}{2} \right) , \\ \langle N_{out}(t_k) \rangle &= [1 - R_{mem}(t_k)] \langle N_{in}(t_k) \rangle .\end{aligned}\quad (13)$$

From an experimental point of view, there could be some error in the setting of  $\phi$  for the MZIs. In particular, we can model the real set phase as

$$\phi_{real} = \phi_{theo} + \delta\phi_{sta} + \delta\phi_{err} , \quad (14)$$

where  $\phi_{theo} = 2 \arcsin \sqrt{R}$  is the ideal value of  $\phi$ , while  $\delta\phi_{sta}$  and  $\delta\phi_{err}$  represent a systematic static offset (due to calibration errors) and stochastic noise (due to temperature or current fluctuations), respectively. Another source of non-ideality is the polarization of the photons entering the chip. The integrated components are designed to work with TE light. Polarization components different from TE lead to non-ideal behaviours. In particular, they eventually affect the visibilities of the MZIs. Therefore, in practice we can model  $R$  as an effective reflectivity given by

$$R = \frac{1}{2} [1 - V \cos(\phi_{real})] , \quad (15)$$

where  $V$  is the visibility of the interference fringe associated to one MZI.  $V$  can be extracted from the calibration data together with a confidence interval. Finally, we have to deal with non-idealities due to dark counts, noise and detector efficiency.

Therefore, we can model the non-idealities as follows

$$\begin{aligned}\langle N_{in}(t_k) \rangle &= \frac{1}{2} [1 - V_{in} \cos(\phi_{\text{real}}^{in}(t_k))] , \\ \langle N_{out}(t_k) \rangle &= \eta [1 - R_{mem}(t_k)] \langle N_{in}(t_k) \rangle + N_{\text{dark}} + \xi_{\text{err}}(t_k) ,\end{aligned}\quad (16)$$

where  $R_{mem}$  is given by Eq. (15),  $\eta$  is the detector efficiency,  $N_{\text{dark}}$  represents dark counts and  $\xi_{\text{err}}$  is stochastic noise.

The simulated results shown in Fig. 3 and Fig. 4 are obtained by putting to zero the stochastic noises and using the parameters reported in Table 2 and Table 3, respectively. These parameters are found through an optimization routine by keeping the visibilities bounded by the value founded in the calibration routine and the static systematic phase error of the order of 0.1 rad. Each row of the two tables corresponds to a different experiment and a different calibration of the phase shifters.

Table 2: Parameters used for the simulated results of a single memristor shown in Fig. 3. The superscripts (0) and (M1) stand for MZI-0 and MZI-M1, respectively. The static systematic phase errors  $\delta\phi_{\text{sta}}$  are measured in radians. The parameters are rounded to the second decimal place.

	$V^{(0)}$	$V^{(M1)}$	$\delta\phi_{\text{sta}}^{(0)}$	$\delta\phi_{\text{sta}}^{(M1)}$
$T = 0.01 T_{\text{osc}}$	0.99	0.83	-0.03	-0.11
$T = 0.1 T_{\text{osc}}$	1.00	0.82	0.05	-0.20
$T = 0.3 T_{\text{osc}}$	1.00	0.92	0.03	0.09
$T = 0.5 T_{\text{osc}}$	0.95	0.92	0.00	0.03
$T = 0.7 T_{\text{osc}}$	0.93	0.80	0.17	-0.16
$T = T_{\text{osc}}$	0.99	0.90	0.12	-0.20

Table 3: Parameters used for the simulated results of the coupled memristors shown in Fig. 4. The superscripts (0), (1), (2), (M1) and (M2) stand for MZI-0, MZI-1, MZI-2, MZI-M1 and MZI-M2, respectively. The static systematic phase errors  $\delta\phi_{\text{sta}}$  are measured in radians. The parameters are rounded to the second decimal place.

	$V^{(0)}$	$V^{(1)}$	$V^{(2)}$	$V^{(M1)}$	$V^{(M2)}$	$\delta\phi_{\text{sta}}^{(1)}$	$\delta\phi_{\text{sta}}^{(2)}$	$\delta\phi_{\text{sta}}^{(M1)}$	$\delta\phi_{\text{sta}}^{(M2)}$
$T = 0.2 T_{\text{osc}}$ and $\Phi = 0.7 \text{ rad}$	0.95	0.83	0.89	0.95	0.91	-0.16	-0.02	0.03	-0.02
$T = 0.3 T_{\text{osc}}$ and $\Phi = 0.5 \text{ rad}$	1.00	0.90	0.95	1.00	0.87	-0.10	-0.19	-0.01	-0.02
$T = 0.4 T_{\text{osc}}$ and $\Phi = 0.7 \text{ rad}$	0.95	0.92	0.97	1.00	0.89	-0.20	-0.02	0.01	0.00

## References

- [1] Y. LeCun, Y. Bengio, and G. Hinton. “Deep learning”. In: *nature* 521.7553 (2015), pp. 436–444.
- [2] H. Ismail Fawaz, G. Forestier, J. Weber, L. Idoumghar, and P.-A. Muller. “Deep learning for time series classification: a review”. In: *Data mining and knowledge discovery* 33.4 (2019), pp. 917–963.
- [3] H. A. Pierson and M. S. Gashler. “Deep learning in robotics: a review of recent research”. In: *Advanced Robotics* 31.16 (2017), pp. 821–835.
- [4] H.-Y. Huang, M. Broughton, J. Cotler, S. Chen, J. Li, M. Mohseni, H. Neven, R. Babbush, R. Kueng, J. Preskill, et al. “Quantum advantage in learning from experiments”. In: *Science* 376.6598 (2022), pp. 1182–1186.
- [5] J. Gao, L.-F. Qiao, Z.-Q. Jiao, Y.-C. Ma, C.-Q. Hu, R.-J. Ren, A.-L. Yang, H. Tang, M.-H. Yung, and X.-M. Jin. “Experimental Machine Learning of Quantum States”. In: *Phys. Rev. Lett.* 120 (24 2018), p. 240501. DOI: [10.1103/PhysRevLett.120.240501](https://doi.org/10.1103/PhysRevLett.120.240501).
- [6] G. Carleo, I. Cirac, K. Cranmer, L. Daudet, M. Schuld, N. Tishby, L. Vogt-Maranto, and L. Zdeborová. “Machine learning and the physical sciences”. In: *Reviews of Modern Physics* 91.4 (2019), p. 045002.
- [7] J. Biamonte, P. Wittek, N. Pancotti, P. Rebentrost, N. Wiebe, and S. Lloyd. “Quantum machine learning”. In: *Nature* 549.7671 (2017), pp. 195–202.
- [8] Y. Du, M.-H. Hsieh, and D. Tao. “Efficient learning for linear properties of bounded-gate quantum circuits”. In: *Nature Communications* 16.1 (2025), p. 3790.
- [9] Y. Mo, L. Zhang, Y.-A. Chen, Y. Liu, T. Lin, and X. Wang. “Parameterized quantum comb and simpler circuits for reversing unknown qubit-unitary operations”. In: *npj Quantum Information* 11.1 (2025), p. 32.
- [10] S. Jerbi, C. Gyurik, S. C. Marshall, R. Molteni, and V. Dunjko. “Shadows of quantum machine learning”. In: *Nature Communications* 15.1 (2024), p. 5676.
- [11] V. Saggio, B. E. Asenbeck, A. Hamann, T. Strömbärg, P. Schiansky, V. Dunjko, N. Friis, N. C. Harris, M. Hochberg, D. Englund, et al. “Experimental quantum speed-up in reinforcement learning agents”. In: *Nature* 591.7849 (2021), pp. 229–233.
- [12] E. Knill, R. Laflamme, and G. J. Milburn. “A scheme for efficient quantum computation with linear optics”. In: *nature* 409.6816 (2001), pp. 46–52.
- [13] S. Scheel, K. Nemoto, W. J. Munro, and P. L. Knight. “Measurement-induced nonlinearity in linear optics”. In: *Physical Review A* 68.3 (2003), p. 032310.
- [14] X. Zhou and A. Mizel. “Nonlinear coupling of nanomechanical resonators to Josephson quantum circuits”. In: *Physical review letters* 97.26 (2006), p. 267201.
- [15] B. Hacker, S. Welte, G. Rempe, and S. Ritter. “A photon–photon quantum gate based on a single atom in an optical resonator”. In: *Nature* 536.7615 (2016), pp. 193–196.
- [16] A. Javadi, I. Söllner, M. Arcari, S. L. Hansen, L. Midolo, S. Mahmoodian, G. Kiršanskė, T. Pagnolato, E. Lee, J. Song, et al. “Single-photon non-linear optics with a quantum dot in a waveguide”. In: *Nature communications* 6.1 (2015), p. 8655.
- [17] M. Heuck, K. Jacobs, and D. R. Englund. “Controlled-Phase Gate Using Dynamically Coupled Cavities and Optical Nonlinearities”. In: *Phys. Rev. Lett.* 124 (16 2020), p. 160501. DOI: [10.1103/PhysRevLett.124.160501](https://doi.org/10.1103/PhysRevLett.124.160501).
- [18] L. O. Chua. “Memristor – The Missing Circuit Element”. In: *IEEE Transactions on Circuit Theory* 18.5 (1971), pp. 507–519. DOI: [10.1109/TCT.1971.1083337](https://doi.org/10.1109/TCT.1971.1083337).

[19] M. Di Ventra and Y. V. Pershin. *Memristors and Memelements*. Springer, 2023. URL: <https://link.springer.com/book/10.1007/978-3-031-25625-7>.

[20] A. Emboras, A. Alabastri, P. Lehmann, K. Portner, C. Weilenmann, P. Ma, B. Cheng, M. Lewerenz, E. Passerini, U. Koch, J. Aeschlimann, F. Ducry, J. Leuthold, and M. Luisier. “Opto-electronic memristors: Prospects and challenges in neuromorphic computing”. In: *Applied Physics Letters* 117.23 (Dec. 2020), p. 230502. ISSN: 0003-6951. DOI: 10.1063/5.0028539.

[21] S. Kumar, X. Wang, J. P. Strachan, Y. Yang, and W. D. Lui. “Dynamical memristors for higher-complexity neuromorphic computing”. In: *Nature Reviews Materials* 7.7 (2022), pp. 575–591.

[22] P. Pfeiffer, I. L. Egusquiza, M. Di Ventra, M. Sanz, and E. Solano. “Quantum memristors”. en. In: *Scientific Reports* 6.1 (2016), p. 29507. ISSN: 2045-2322. DOI: 10.1038/srep29507.

[23] J. Salmilehto, F. Deppe, M. Di Ventra, M. Sanz, and E. Solano. “Quantum Memristors with Superconducting Circuits”. en. In: *Scientific Reports* 7.1 (2017), p. 42044. ISSN: 2045-2322. DOI: 10.1038/srep42044.

[24] S. Y. Stremoukhov, P. A. Forsh, K. Y. Khabarova, and N. N. Kolachevsky. “Model of Coupled Quantum Memristors Based on a Single Trapped  $^{171}\text{Yb}^+$  Ion”. en. In: *JETP Letters* 119.5 (2024), pp. 352–356. ISSN: 0021-3640, 1090-6487. DOI: 10.1134/S0021364024600381.

[25] Y. Li, G. W. Holloway, S. C. Benjamin, G. A. D. Briggs, J. Baugh, and J. A. Mol. “Double quantum dot memristor”. en. In: *Physical Review B* 96.7 (2017), p. 075446. ISSN: 2469-9950, 2469-9969. DOI: 10.1103/PhysRevB.96.075446.

[26] J. Bao, Z. Fu, T. Pramanik, J. Mao, Y. Chi, Y. Cao, C. Zhai, Y. Mao, T. Dai, X. Chen, et al. “Very-large-scale integrated quantum graph photonics”. In: *Nature Photonics* 17.7 (2023), pp. 573–581.

[27] A. Boes, B. Corcoran, L. Chang, J. Bowers, and A. Mitchell. “Status and potential of lithium niobate on insulator (LNOI) for photonic integrated circuits”. In: *Laser & Photonics Reviews* 12.4 (2018), p. 1700256.

[28] S. Slussarenko and G. J. Pryde. “Photonic quantum information processing: A concise review”. In: *Applied physics reviews* 6.4 (2019).

[29] J.-H. Kim, S. Aghaeimeibodi, J. Carolan, D. Englund, and E. Waks. “Hybrid integration methods for on-chip quantum photonics”. In: *Optica* 7.4 (2020), pp. 291–308.

[30] J. Gao, X.-W. Wang, W.-H. Zhou, Z.-Q. Jiao, R.-J. Ren, Y.-X. Fu, L.-F. Qiao, X.-Y. Xu, C.-N. Zhang, X.-L. Pang, H. Li, Y. Wang, and X.-M. Jin. “Quantum advantage with membosonsampling”. In: *Chip* 1.2 (2022), p. 100007. ISSN: 2709-4723. DOI: <https://doi.org/10.1016/j.chip.2022.100007>.

[31] Q. Liu, W. Liu, Y. Jia, K. Ziegler, A. Alù, and F. Chen. “Measurement-induced photonic topological insulators”. In: *Science Advances* 11.29 (2025), eadx0595.

[32] M. Sanz, L. Lamata, and E. Solano. “Quantum memristors in quantum photonics”. en. In: *APL Photonics* 3.8 (2018), p. 080801. ISSN: 2378-0967. DOI: 10.1063/1.5036596.

[33] S. D. Micco, B. Polacchi, T. Giordani, and F. Sciarrino. *Quantum memristor with vacuum-one-photon qubits*. arXiv:2503.02466 [quant-ph]. 2025.

[34] M. Spagnolo, J. Morris, S. Piacentini, M. Antesberger, F. Massa, A. Crespi, F. Ceccarelli, R. Osellame, and P. Walther. “Experimental photonic quantum memristor”. In: *Nature Photonics* 16.4 (2022), pp. 318–323.

[35] K. Luke, Y. Okawachi, M. R. Lamont, A. L. Gaeta, and M. Lipson. “Broadband mid-infrared frequency comb generation in a  $\text{Si}_3\text{N}_4$  microresonator”. In: *Optics letters* 40.21 (2015), pp. 4823–4826.

[36] C. Wang, M. Zhang, X. Chen, M. Bertrand, A. Shams-Ansari, S. Chandrasekhar, P. Winzer, and M. Lončar. “Integrated lithium niobate electro-optic modulators operating at CMOS-compatible voltages”. In: *Nature* 562.7725 (2018), pp. 101–104.

[37] M. He, M. Xu, Y. Ren, J. Jian, Z. Ruan, Y. Xu, S. Gao, S. Sun, X. Wen, L. Zhou, et al. “High-performance hybrid silicon and lithium niobate Mach–Zehnder modulators for 100 Gbit s<sup>-1</sup> and beyond”. In: *Nature photonics* 13.5 (2019), pp. 359–364.

[38] S. Lindner, N. Rahbany, C. Pauly, L. Gines, S. Mandal, O. A. Williams, A. Muzha, A. Krueger, R. Bachelot, C. Couteau, et al. “Coupling of single nanodiamonds hosting SiV color centers to plasmonic double bowtie microantennas”. In: *Nanotechnology* 36.13 (2025), p. 135001.

[39] K. Ngan, Y. Zhan, C. Dory, J. Včković, and S. Sun. “Quantum photonic circuits integrated with color centers in designer nanodiamonds”. In: *Nano Letters* 23.20 (2023), pp. 9360–9366.

[40] K. G. Fehler, A. P. Ovyyan, L. Antoniuk, N. Lettner, N. Gruhler, V. A. Davydov, V. N. Agafonov, W. H. Pernice, and A. Kubanek. “Purcell-enhanced emission from individual SiV- center in nanodiamonds coupled to a Si3N4-based, photonic crystal cavity”. In: *Nanophotonics* 9.11 (2020), pp. 3655–3662.

[41] A. Berezhnoi, A. Zakirov, and A. Kalachev. “Quantum memory based on SiV-centers in nanodiamonds”. In: *Laser Physics Letters* 19.12 (2022), p. 125206.

[42] B. Pingault, D.-D. Jarausch, C. Hepp, L. Klintberg, J. N. Becker, M. Markham, C. Becher, and M. Atatüre. “Coherent control of the silicon-vacancy spin in diamond”. In: *Nature communications* 8.1 (2017), p. 15579.

[43] D. D. Sukachev, A. Sipahigil, C. T. Nguyen, M. K. Bhaskar, R. E. Evans, F. Jelezko, and M. D. Lukin. “Silicon-vacancy spin qubit in diamond: a quantum memory exceeding 10 ms with single-shot state readout”. In: *Physical review letters* 119.22 (2017), p. 223602.

[44] C. Nguyen, D. Sukachev, M. Bhaskar, B. Machielse, D. Levonian, E. Knall, P. Stroganov, R. Riedinger, H. Park, M. Lončar, et al. “Quantum network nodes based on diamond qubits with an efficient nanophotonic interface”. In: *Physical review letters* 123.18 (2019), p. 183602.

[45] S. Kumar, F. A. Cárdenas-López, N. N. Hegade, X. Chen, F. Albarrán-Arriagada, E. Solano, and G. Alvarado Barrios. “Entangled quantum memristors”. en. In: *Physical Review A* 104.6 (2021), p. 062605. ISSN: 2469-9926, 2469-9934. DOI: 10.1103/PhysRevA.104.062605.

[46] S. Kumar, F. Cárdenas-López, N. Hegade, F. Albarrán-Arriagada, E. Solano, and G. A. Barrios. “Tripartite Entanglement in Quantum Memristors”. en. In: *Physical Review Applied* 18.3 (2022), p. 034004. ISSN: 2331-7019. DOI: 10.1103/PhysRevApplied.18.034004.

[47] A. Ferrara and R. Lo Franco. “Entanglement and coherence dynamics in photonic quantum memristors”. en. In: *Physical Review A* 111.1 (2025), p. 012421. ISSN: 2469-9926, 2469-9934. DOI: 10.1103/PhysRevA.111.012421.

[48] M. Selimović, I. Agresti, M. Siemaszko, J. Morris, B. Dakić, R. Albiero, A. Crespi, F. Cecarelli, R. Osellame, M. Stobińska, and P. Walther. *Experimental neuromorphic computing based on quantum memristor*. arXiv:2504.18694 [quant-ph]. 2025.

[49] A. Sakurai, A. Hayashi, W. J. Munro, and K. Nemoto. “Quantum optical reservoir computing powered by boson sampling”. In: *Optica Quantum* 3.3 (2025), pp. 238–245.

[50] G. R. Steinbrecher, J. P. Olson, D. Englund, and J. Carolan. “Quantum optical neural networks”. In: *npj Quantum Information* 5.1 (2019), p. 60.

[51] G. Thiering and A. Gali. “Color centers in diamond for quantum applications”. In: *Annual Review of Condensed Matter Physics* 11 (2020), pp. 1–27. DOI: [10.1146/annurev-conmatphys-031218-013615](https://doi.org/10.1146/annurev-conmatphys-031218-013615).

[52] M. W. Doherty, N. B. Manson, P. Delaney, F. Jelezko, J. Wrachtrup, and L. C. L. Hollenberg. “The nitrogen-vacancy colour centre in diamond”. In: *Physics Reports* 528.1 (2013), pp. 1–45. DOI: [10.1016/j.physrep.2013.02.001](https://doi.org/10.1016/j.physrep.2013.02.001).

[53] S Lagomarsino, A. Flatae, H Kambalathmana, F Sledz, L Hunold, N Soltani, P Reuschel, S Sciortino, N Gelli, M Massi, et al. “Creation of silicon-vacancy color centers in diamond by ion implantation”. In: *Frontiers in Physics* 8 (2021), p. 601362.

[54] C. Bradac, W. Gao, J. Forneris, M. E. Trusheim, and I. Aharonovich. “Quantum nanophotonics with group IV defects in diamond”. In: *Nature communications* 10.1 (2019), p. 5625.

[55] S. Lagomarsino, V. Agafonov, M. Cialone, P. Olivero, et al. “Creation of Silicon-Vacancy Color Centers in Diamond”. In: *Frontiers in Physics* 8 (2021), p. 601362. DOI: [10.3389/fphy.2020.601362](https://doi.org/10.3389/fphy.2020.601362).

[56] S. Lindner, F. Dortat, S. Gsell, S. Greulich-Weber, and E. Neu. “Strongly inhomogeneous distribution of spectral properties of silicon-vacancy centers in nanodiamonds”. In: *Physical Review B* 98.7 (2018), p. 075302. DOI: [10.1103/PhysRevB.98.075302](https://doi.org/10.1103/PhysRevB.98.075302).

[57] L. Chua and S. M. Kang. “Memristive devices and systems”. In: *Proceedings of the IEEE* 64.2 (1976), pp. 209–223. DOI: [10.1109/PROC.1976.10092](https://doi.org/10.1109/PROC.1976.10092).

[58] D. B. Strukov, G. S. Snider, D. R. Stewart, and R. S. Williams. “The missing memristor found”. In: *Nature* 453.7191 (2008), pp. 80–83. DOI: [10.1038/nature06932](https://doi.org/10.1038/nature06932).

[59] M. Di Ventra, Y. V. Pershin, and L. O. Chua. “Circuit Elements With Memory: Memristors, Memcapacitors, and Meminductors”. In: *Proceedings of the IEEE* 97.10 (2009), pp. 1717–1724. DOI: [10.1109/JPROC.2009.2021077](https://doi.org/10.1109/JPROC.2009.2021077).

[60] L. Soldano and E. C. M. Pennings. “Optical multi-mode interference devices based on self-imaging: principles and applications”. In: *Journal of Lightwave Technology* 13 (1995), pp. 615–627.

[61] N. C. Harris, Y. Ma, J. Mower, T. Baehr-Jones, D. Englund, M. Hochberg, and C. Galland. “Efficient, compact and low loss thermo-optic phase shifter in silicon”. In: *Opt. Express* 22.9 (2014), pp. 10487–10493. DOI: [10.1364/OE.22.010487](https://doi.org/10.1364/OE.22.010487).

[62] A. Baldazzi, N. Leone, M. Sanna, S. Azzini, and L. Pavesi. “A linear photonic swap test circuit for quantum kernel estimation”. In: *Quantum Science and Technology* 9.4 (2024), p. 045053.

[63] A. Issa, I. Izquierdo, M. Merheb, D. Ge, A. Broussier, N. Ghabri, S. Marguet, C. Couteau, R. Bachelot, and S. Jradi. “One Strategy for Nanoparticle Assembly onto 1D, 2D, and 3D Polymer Micro and Nanostructures”. In: *ACS Applied Materials & Interfaces* 13.35 (2021), pp. 41846–41856. DOI: [10.1021/acsami.1c03905](https://doi.org/10.1021/acsami.1c03905).

[64] T. Ritacco, A. Issa, R. Beccherelli, S. Jradi, and R. Bachelot. “Quantum Dot-Polymer Architectures by Two-Photon Polymerization: From 4D Microfabrication to Quantum Light Sources”. In: *Advanced Optical Materials* 13.29 (2025), e03288. DOI: <https://doi.org/10.1002/adom.202403288>.

[65] J. Arjona Martínez, R. A. Parker, K. C. Chen, C. M. Purser, L. Li, C. P. Michaels, A. M. Stramma, R. Debroux, I. B. Harris, M. Hayhurst Appel, E. C. Nichols, M. E. Trusheim, D. A. Gangloff, D. Englund, and M. Atatüre. “Photonic Indistinguishability of the Tin-Vacancy Center in Nanostructured Diamond”. In: *Phys. Rev. Lett.* 129 (17 2022), p. 173603. DOI: [10.1103/PhysRevLett.129.173603](https://doi.org/10.1103/PhysRevLett.129.173603).

- [66] N. Somaschi, V. Giesz, L. De Santis, J. C. Loredo, M. P. Almeida, G. Hornecker, S. L. Portalupi, T. Grange, C. Antón, J. Demory, C. Gómez, I. Sagnes, N. D. Lanzillotti-Kimura, A. Lemaître, A. Auffeves, A. G. White, L. Lanco, and P. Senellart. “Near-optimal single-photon sources in the solid state”. In: *Nature Photonics* 10.5 (Mar. 2016), 340–345. ISSN: 1749-4893. DOI: [10.1038/nphoton.2016.23](https://doi.org/10.1038/nphoton.2016.23).
- [67] F. Ceccarelli, S. Atzeni, C. Pentangelo, F. Pellegatta, A. Crespi, and R. Osellame. “Low Power Reconfigurability and Reduced Crosstalk in Integrated Photonic Circuits Fabricated by Femtosecond Laser Micromachining”. In: *Photonics Reviews* 14.10 (Aug. 2020). ISSN: 1863-8899. DOI: [10.1002/1por.202000024](https://doi.org/10.1002/1por.202000024).
- [68] M. Reck, A. Zeilinger, H. J. Bernstein, and P. Bertani. “Experimental realization of any discrete unitary operator”. In: *Physical Review Letters* 73.1 (1994), pp. 58–61. DOI: [10.1103/PhysRevLett.73.58](https://doi.org/10.1103/PhysRevLett.73.58).
- [69] W. R. Clements, P. C. Humphreys, B. J. Metcalf, W. S. Kolthammer, and I. A. Walmsley. “Optimal design for universal multiport interferometers”. In: *Optica* 3.12 (2016), pp. 1460–1465. ISSN: 2334-2536. DOI: [10.1364/OPTICA.3.001460](https://doi.org/10.1364/OPTICA.3.001460).